Measurement of the Parity Violating Asymmetry in the $N \rightarrow \Delta$ Transition (Originally E97-104)

S.P. Wells (cospokesman), N. Simicevic (cospokesman), K. Johnston, and T.A. Forest
Center for Applied Physics Studies
Louisiana Tech University
Ruston, Louisiana 71272
and
The G0 Collaboration
California Institute of Technology
Carnegie-Mellon University
College of William and Mary
Hampton University
IPN Orsay
ISN Grenoble
Louisiana Tech University
New Mexico State University
TJNAF
TRIUMF
University of Connecticut
University of Illinois
University of Kentucky
University of Manitoba
University of Maryland
University of Massachusetts
University of Northern British Columbia
Virginia Tech University
Yerevan Physics Institute

1 Introduction

This proposal has been prepared for the review of the "Parity Violating Asymmetry in the $N \rightarrow \Delta$ Transition" experiment by the Jefferson Lab Program Advisory Committee. This experiment was previously approved as experiment E97-104 with a B^+ priority in February 1997 by PAC13, and was conditionally approved as experiment E01-115 with a B^+ priority at PAC20. This experiment uses the G0 apparatus in its backward angle mode of running, and will acquire data during the same running period as the G0 elastic measurements are made.

In this experiment, the parity violating asymmetry in inclusive single pion electroproduction from the proton will be measured over a squared four momentum transfer range of $0.1 \leq Q^2 \leq 0.6$ $(\mathrm{GeV/c})^2$. These measurements will be made with the same equipment as the G0 backward angle measurements are made, and during the same running period as the G0 backward angle

measurements, so that no additional resources or beam time are required beyond those allocated for G0 backward angle running. The primary purpose of this experiment is to extract the axial vector transition form factor $G_{N\Delta}^{A}$ for the $N \rightarrow \Delta$ transition as a function of Q^2. This form factor characterizes the axial, or intrinsic spin response of the nucleon during its transition to its first excited state. The proposed measurements represent the first determination of this quantity in the neutral current sector of the weak interaction, and in a Q^2 range that is complementary to other experiments (with Q^2 coverage $0.5 \leq Q^2 \leq 2.5$ $(\mathrm{GeV/c})^2$) which use exclusive electroproduction of the Δ^{++} resonance, along with assumptions of PCAC and extrapolations of low energy theorems, to extract the charged current analog of this form factor. In addition to the extraction of $G_{N\Delta}^{A}$, these measurements of the inelastic asymmetry will constrain the contribution of inelastic electrons to the elastic parity violating asymmetry, which is the primary goal of the G0 program.

A review of the physics motivation and formalism and theoretical work is provided in the next section, including an update of new theoretical work completed and the implications for these proposed measurements. In this section we will present our expected uncertainties, and what impact they will have on theory as it presently exists. This is followed by a summary of the experimental configuration to be used and a detailed discussion of the cross section and rate calculations and expected backgrounds.

2 Scientific Justification and Formalism

The coupling of electrons to quarks in the nucleon through the exchange of a Z^0 boson is represented by a first order Feynman diagram for this exchange between an electron with four momentum K and target nucleon with four momentum P, as shown in Fig. 1.

The momentum of the scattered electron is K', and the momentum and of the other outgoing particle is P'. The electron couples to the Z^0 boson according to

$$\langle K'|j_{\mu}^{Z}|K\rangle \;=\; \bar{u}(K')[g_{V,e}\gamma_{\mu} + g_{A,e}\gamma_{\mu}\gamma_{5}]u(K) \tag{1}$$

showing explicitly the vector-axial vector structure of the weak neutral current interaction. The vector and axial-vector couplings ($g_{V,e}$ and $g_{A,e}$) are functions of standard model parameters,

$$g_{V,e} = \frac{-e}{4\sin\theta_W\cos\theta_W}(1 - 4\sin^2\theta_W)$$

$$g_{A,e} = \frac{e}{4\sin\theta_W\cos\theta_W}(1 - 2\sin^2\theta_W).$$

For the Z^0-nucleon coupling, the weak neutral current takes on different forms for the elastic and inelastic channels. In the elastic channel, we have

$$\langle P'|J_{\mu}^{Z}|P\rangle \;=\; \bar{u}(P')[\gamma_{\mu}F_1^Z + i\frac{\sigma_{\mu\nu}q^{\nu}}{2M}F_2^Z + \gamma_{\mu}\gamma_5 G_A^Z]u(P) \tag{2}$$

where, again, the vector-axial vector nature of the weak neutral current is evident. The neutral weak vector (F_1^Z,F_2^Z) and axial vector (G_A^Z) form factors of the nucleon (which are functions only of Q^2) can be expressed in terms of the individual quark form factors [1]; it is through these

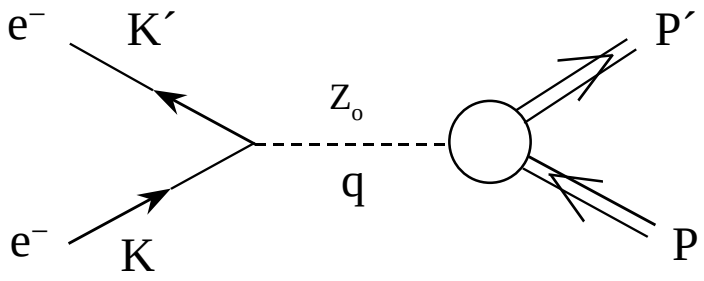

Figure 1: Feynman diagram for Z^0 exchange

weak neutral form factors, when combined with the nucleon electromagnetic form factors, that the strange quark content of the nucleon can be accessed.

In the inelastic Δ channel, the neutral current is somewhat more complicated in its general form [2],

$$\begin{aligned}\langle P'|J^Z_\mu|P\rangle \;=\; & \bar{U}^\lambda(P')[(\tfrac{C^Z_{3V}}{M}\gamma^\nu + \tfrac{C^Z_{4V}}{M^2}P'^\nu + \tfrac{C^Z_{5V}}{M^2}P^\nu)(g_{\lambda\mu}g_{\rho\nu} - g_{\lambda\rho}g_{\mu\nu})q^\rho\gamma_5 \\ & +\; C^Z_{6V}g_{\lambda\mu}\gamma_5 + (\tfrac{C^Z_{3A}}{M}\gamma^\nu + \tfrac{C^Z_{4A}}{M^2}P'^\nu)(g_{\lambda\mu}g_{\rho\nu} - g_{\lambda\rho}g_{\mu\nu})q^\rho \\ & +\; C^Z_{5A}g_{\lambda\mu} + \tfrac{C^Z_{6A}}{M^2}P_\lambda q_\mu)]u(P) \end{aligned} \tag{3}$$

but the vector-axial vector nature can still be seen. In this expression, $U^\lambda(P')$ is the Rarita-Schwinger field describing the spin-$\frac{3}{2}$ Δ resonance [3], P and P' are, respectively, the momenta of the nucleon and the Δ, and $q \;=\; P' - P$.

It has been argued [4] that the weak transition form factors in Eq. (3) (C^Z_{iV} and C^Z_{iA}), which are functions only of Q^2, can be related to the electroproduction and weak charged current production of the Δ by performing a rotation in isospin space and exploiting the conserved vector current (CVC) hypothesis [2]. In the notation of Llewellyn-Smith [4], they become

$$\begin{aligned} C^Z_{iV} &= \alpha C^\gamma_i, \quad i = 3,4,5\ , \\ C^Z_{6V} &= 0\ , \\ C^Z_{iA} &= -\beta C^A_i, \quad i = 3,4,5,6\ , \end{aligned} \tag{4}$$

where α and β are the quark-Z^0 couplings

$$\alpha = \frac{e}{2\sin\theta_W\cos\theta_W}(1 - 2\sin^2\theta_W)$$

$$\beta = \frac{-e}{2\sin\theta_W\cos\theta_W}.$$

The electroproduction form factors are denoted by C^γ_i, and C^A_i are $-\frac{1}{\sqrt{3}}$ times the charged-current axial vector weak transition form factors. Presently, there exist considerable data on the vector current transistion form factors C^γ_i which have been obtained with electromagnetic probes. A comparison of these experimentally determined quantities to theoretical predictions points to significant disagreement (see Ref. [5]). Both lattice QCD calculations [6] and spin-flavor SU(6) based constituent quark models [7], for example, underpredict the data by $\sim 30\%$. In contrast, only a limited amount of data exist for the axial transition form factors C^A_i, obtained from charged current experiments, and these data have considerably larger uncertainties than the vector current form factors. Despite these larger uncertainties, QCD inspired models and a recently completed cloudy bag model [8], tend to underpredict the central values for the axial matrix elements by $\sim 30\%$, just as for the vector form factors. Thus, a more precise determination of the axial transition form factor, as described in this proposal, will considerably sharpen our present knowledge of the axial vector transition amplitude.

2.1 Axial Transition Form Factor

In order to connect the parity violating asymmetry in the $N \to \Delta$ transition to these form factors, we make the isospin structure of this transition evident. To this end, it is useful to

examine the parity violating phenomenological Lagrangian for electron nucleon scattering [9],

$$\begin{aligned} L &= -\frac{G_F}{2}\{\bar{e}\gamma_\lambda\gamma_5 e[\frac{\tilde{\alpha}}{2}(\bar{u}\gamma_\lambda u - \bar{d}\gamma_\lambda d) + \frac{\tilde{\gamma}}{2}(\bar{u}\gamma_\lambda u + \bar{d}\gamma_\lambda d)] \\ &+ \bar{e}\gamma_\lambda e[\frac{\tilde{\beta}}{2}(\bar{u}\gamma_\lambda\gamma_5 u - \bar{d}\gamma_\lambda\gamma_5 d) + \frac{\tilde{\delta}}{2}(\bar{u}\gamma_\lambda\gamma_5 u + \bar{d}\gamma_\lambda\gamma_5 d) + ...]\}, \end{aligned} \tag{5}$$

where $(\bar{e}, e)$, $(\bar{u}, u)$, and $(\bar{d}, d)$ represent Dirac spinors for the electrons and quarks, the electron-quark coupling constants have the following meaning:

$\tilde{\alpha}$: isovector axial vector electron – vector quark,

$\tilde{\beta}$: isovector vector electron – axial vector quark,

$\tilde{\gamma}$: isoscalar axial vector electron – vector quark,

$\tilde{\delta}$: isoscalar vector electron – axial vector quark,

with standard model relations

$$\tilde{\alpha} = -(1 - 2\sin^2\theta_W)$$

$$\tilde{\beta} = -(1 - 4\sin^2\theta_W)$$

$$\tilde{\gamma} = \frac{2}{3}\sin^2\theta_W$$

$$\tilde{\delta} = 0.$$

The dots in Eq. (5) denote isoscalar axial currents for the four remaining quark flavors.

To the extent that the $N \to \Delta$ transition is purely isovector, the parity violating asymmetry for Δ production takes the form [10]

$$A_{RL} = \frac{d\sigma_R - d\sigma_L}{d\sigma_R + d\sigma_L} = \frac{G_F}{\sqrt{2}}\frac{Q^2}{2\pi\alpha}[\tilde{\alpha} + \tilde{\beta}F(Q^2, E, E', \theta_e)], \tag{6}$$

where $d\sigma_{R(L)} \equiv \frac{d^2\sigma}{dq^2 dW^2}|_{R(L)}$ is the differential cross section for scattering electrons of positive (negative) helicity from the nucleon, $Q^2 = -(K - K')^2$, $W^2 = (P + K - K')^2$, α in this case is the electromagnetic coupling constant, and $F(Q^2, E, E', \theta_e)$ contains all of the weak transition form factors discussed above, and dependence on kinematic variables. Specifically, we write (see Appendix A),

$$F(Q^2, E, E', \theta_e) = \frac{(E + E')}{M}H^{EM}(Q^2, \theta_e)G^A_{N\Delta}(Q^2), \tag{7}$$

where $H^{EM}(Q^2, \theta_e)$ contains the electromagnetic form factors $C^\gamma_i(Q^2)$ $(i = 3, 4)$, and $G^A_{N\Delta}(Q^2)$ contains the axial transition form factors $C^A_i(Q^2)$ $(i = 3, 4, 5, 6)$. Thus, for a pure isovector $N \to \Delta$ transition, the parity violating asymmetry consists of two terms: the axial vector electron-vector quark coupling, which is given explicitly by the electron-quark coupling constant $\tilde{\alpha}$, and the vector electron-axial vector quark coupling, which contains the axial vector transition form

factor $G^A_{N\Delta}$. The relative strengths of these two terms is determined by the coupling constants $\tilde{\alpha}$ and $\tilde{\beta}$, which, with the standard model value of $\sin^2\theta_W$=0.2122, take on the numerical values

$$\tilde{\alpha} \;=\; -0.5756 \;\;,\;\; \tilde{\beta} \;=\; -0.1512.$$

Thus, for reasonable $F(Q^2, E, E', \theta_e)$ values, the leading $\tilde{\alpha}$ term contributes roughly 75% to this parity violating asymmetry. Using estimates for the $N \rightarrow \Delta$ weak transition form factors, $F(Q^2, E, E', \theta_e)$ is found to be of order unity in this kinematic regime [10], in contrast to the high energy limit ($\frac{Q^2}{2ME} \ll 1$), where $F(Q^2, E, E', \theta_e) \ll 1$ [11]. Consequently, using relatively low beam energies and detecting electrons scattered at backward angles, as is planned for these measurements, enhances our sensitivity to the $N \rightarrow \Delta$ axial transition form factor $G^A_{N\Delta}(Q^2)$.

The charged current analog of this form factor can be accessed in a number of different ways, and is usually parameterized in terms of the axial-vector mass M_A, according to the Adler model [12], in which a modified dipole form is used. In neutrino induced weak Δ^{++} production, the charged current version of $G^A_{N\Delta}(Q^2)$ can be determined through the Q^2 dependence of the differential cross section for this reaction, and therefore represents a determination of this form factor in the charged current sector of the weak interaction. An early study of neutrino induced weak Δ^{++} production from the proton [13] yielded a value of $M_A = 0.95 \pm 0.09$. A more recent study [14] of this reaction on deuterium between $0.1 \leq Q^2 \leq 3.0$ (GeV/c)^2 yielded $M_A = 1.28^{+0.08}_{-0.10}$, but this value showed sensitivities to deuteron structure and cuts on spectator nucleon momentum. The measurements described in this report will provide the first determination of M_A in the neutral current sector. Because the measurements described here result from the neutral weak interaction, where a Z_0 boson induces the transition to the Δ^+ resonance, $G^A_{N\Delta}(Q^2)$ respresents the weak analog of the M1 photon induced magnetic spin flip transition amplitude, and in a quark model picture, would result from the Z_0 boson flipping the spin of one of the nucleon's consitutent quarks. In contrast, in neutrino induced Δ^{++} reactions a flavor change is required to create the Δ^{++}, and therefore represents a completely different reaction mechanism. Thus, a direct comparison of the Q^2 dependence of the form factors obtained from the different experiments may not be possible, although determination of both would provide a more complete picture of the weak excitation of the nucleon to the Δ excited state. In addition, the determination of M_A from the neutral current measurements described here, when compared to the values of M_A determined from charged current experiments, would ultimately test the assumption that the neutral current form factors are simply related to their charged current analogs through an isospin rotation, despite the vastly different reaction mechanisms required to create the different charge states.

Another experimental technique to access the charged current version of this form factor is through $\pi^-\Delta^{++}$ electroproduction, where coincidence differential cross section measurements are typically performed near threshold [15, 16, 17], in which the scattered e^- and the electroproduced π^- are detected. To interpret these data, low energy theorems are extrapolated from threshold through the resonance region, and use is made of the partially conserved axial vector current (PCAC) hypothesis. To date, data from experiments of this type have instead been interpreted, using the theoretical results of Adler and Weisberger [18], in terms of the nucleon axial vector form factor $G_A(Q^2)$. The TJNAF experiment E94-005 [15], however, will use the above mentioned techniques and approximations to extract $G^A_{N\Delta}$ for larger Q^2 values than considered in this proposal ($0.5 \leq Q^2 \leq 2.5$ (GeV/c)^2). In contrast, the measurement of the parity violating asymmetry in the $N \rightarrow \Delta$ transition proposed here gives direct access to $G^A_{N\Delta}(Q^2)$, without PCAC or extrapolation of low energy theorems, and again resides in the

neutral current sector of the weak interaction where the reaction mechanism is different than that for the charged current experiments.

2.2 Non-Resonant Contributions

While the $N \rightarrow \Delta$ transition is dominated by the isovector resonant contribution, there are non-resonant contributions to this transition as well. Although these asymmetry measurements give us direct access to $G^A_{N\Delta}(Q^2)$, a correct determination of this form factor can only be done if the non-resonant contributions to the asymmetry are small, or understood. A recent analysis of the weak excitation of the Δ^+ [5] paid particular attention to the relative contributions of the non-resonant terms and the axial response. They found that in our kinematic regime of relatively low beam energies and backward electron scattering angles, the ratio of the non-resonant terms to the axial term was small, ranging from of order 10% to 40%, depending on the particular kinematics. Nonetheless, these non-resonant terms contribute, and must be taken into account to properly extract the axial transition form factor. Understanding these nonresonant pieces has also been the subject of recent work [19], where it is demonstrated that these terms can be extracted through polarization observables in the $p(\vec{e}, e'\vec{p})\pi^0$ reaction. Additionally, the inclusion of nonresonant terms proved to be important in a model which was used to describe recent $(e, e'\pi^0)$ data from both Jefferson Lab and MIT-Bates [20]. The physics program in Hall B at Jefferson Lab includes polarization observables in single pion electroproduction reactions, from which a determination of these nonresonant terms will be made at the 5% level [21], which will be sufficient to constrain these contributions to the $N \rightarrow \Delta$ asymmetry measurement at the level required to extract $G^A_{N\Delta}$. A detailed discussion of the non-resonant contribution is given in Appendix B.

2.3 Weak Radiative Corrections

During a thorough investigation of weak radiative corrections to the PV asymmetry in the $N \rightarrow \Delta$ transition, the authors of Ref. [22] uncovered a new type of radiative correction for inelastic reactions that does not contribute to elastic parity violating electron scattering. Although formally originating from the same Feynman diagram describing so called "anapole" contributions (i.e., a photon coupling to a parity violating hadronic vertex), one such radiative correction involves a parity violating $\gamma N\Delta$ electric dipole transition, which has no analog in the elastic channel. As a consequence of Siegert's theorem, the leading component from the contribution of this transition amplitude is Q^2 independent (a $1/Q^2$ from the photon propagator cancels the leading Q^2 dependence from the anapole term) and is proportional to ω ($\omega = E_f - E_i$) times the parity violating electric dipole matrix element, which is characterized by a low energy constant d_Δ, and results in a non-vanishing parity violating asymmetry at $Q^2 = 0$. Thus, a measurement of the parity violating asymmetry in the $N \rightarrow \Delta$ transition at the photon point, or at very low Q^2, henceforth called the Siegert contribution, would provide a direct measurement of the low energy constant d_Δ.

Although introduced in the context of a radiative correction to the PV asymmetry in the $N \rightarrow \Delta$ transition, the quantity d_Δ is tied to interesting physics in its own right. As mentioned above, d_Δ is given by the PV electric dipole matrix element, the same transition which drives the asymmetry parameter in radiative hyperon decays, e.g. $\Sigma^+ \rightarrow p\gamma$. A long standing puzzle in hyperon decay physics has been understanding the large, negative values obtained for these

parameters, which would vanish in the exact SU(3) limit, a result known as Hara's theorem [23]. While typical SU(3) breaking effects are of order $(m_s - m_u)/1\text{GeV} \sim 15\%$, experimentally the asymmetry parameter for $\Sigma^+ \to p\gamma$ is found to be five times larger. The authors of Ref. [24] proposed a solution to this puzzle by including high mass intermediate state resonances $(1/2^-)$, where the weak Lagrangian allows the coupling of both the hyperon and daughter nucleon to the intermediate state resonances, driving the asymmetry parameter to large negative values. This same reaction mechanism was also shown to simultaneously reproduce the s and p wave amplitudes in nonleptonic hyperon decays, which has also been a long standing puzzle in hyperon decay physics. Thus, if the same underlying dynamics is present in the non-strange sector $(\Delta S = 0)$ as is present in the strangeness changing sector $(\Delta S = 1)$, one would expect d_Δ to be enhanced over its natural scale ($g_\pi = 3.8\times10^{-8}$, corresponding to the scale of charged current hadronic PV effects [25, 26]). The authors of [22] estimate that this enhancement may be as large as a factor of 100, corresponding to an asymmetry of ~ 4 ppm, comparable to the size of the effects due to the axial response and therefore easily measurable. Thus, a measurement of this quantity could provide a window into the underlying dynamics of the unexpectedly large QCD symmetry breaking effects seen in hyperon decays. As part of the Q_{weak} program, there are plans to measure the parity violating asymmetry for inelastic electrons at a Q^2 value of 0.028 $(\text{GeV/c})^2$ to constrain their contribution to the elastic parity violating asymmetry from which the weak charge of the proton will be determined.

2.4 Expected Results

As discussed above, two different kinematic regimes for measurements of the PV asymmetry in the $N \to \Delta$ transition provide two different new and interesting physics scenarios. At larger Q^2 (0.1 – 1.0 GeV^2) the axial transition form factor in the neutral current sector of the weak interaction characterizes the reaction mechanism wherein the Z^0 boson "flips" the spin of one of the quarks in the nucleon, and how those spins redistribute themselves during the transition to the Δ resonance. At very low Q^2 (< 0.1 GeV^2), the $N \to \Delta$ asymmetry is dominated by the Siegert contribution, characterized by d_Δ which may provide a window into the underlying dynamics associated with QCD symmetry breaking effects.

This proposal focusses on the $N \to \Delta$ transition at larger Q^2, where the G0 spectrometer in its backward angle mode will be used. During these measurements, both elastically and inelastically scattered electrons will simultaneously be detected, allowing for a determination of strange quark form factors from the elastic events at three different Q^2 values (0.3, 0.5, and 0.8 GeV^2), and a determination of the axial vector transition form factor from the inelastic events over a Q^2 range $0.1 \leq Q^2 \leq 0.6$ GeV^2. From these latter events, neglecting for the moment contributions from electroweak radiative effects (in particular the Q^2 independent Siegert contribution), the expected results can be summarized in Fig.'s 2 and 3. For our estimated expected uncertainties for these measurements, we assume 700 hours of beam at each of three beam energies of 424 MeV, 585 MeV, and 799 MeV, with 80 μA average current and with average polarization 70%. In Fig. 2 we plot the measured asymmetry (normalized to Q^2) as a function of Q^2. Also included in this plot is the prediction of a model [27] based on effective Lagrangians, in which the contributions from the resonant and non-resonant pieces are shown separately, along with the interference between these two contributions. In this Q^2 regime, and in the context of this particular model, the total asymmetry is dominated by the resonant contribution, indicating that a clean interpretation of the measurements can be made in terms of the axial transition

form factor. In Fig. 3, we extract the axial contribution from the full asymmetry, and plot the axial transition form factor, assuming the Adler parameterization, as a function of Q^2. From the expected precision, we will be able to determine the axial mass parameter M_A, which characterizes the Q^2 dependence of this form factor, to an uncertainty of 0.031, which is roughly a factor of three better than the best neutrino results [14], which determine the charge current analog of M_A to an uncertainty of 0.09.

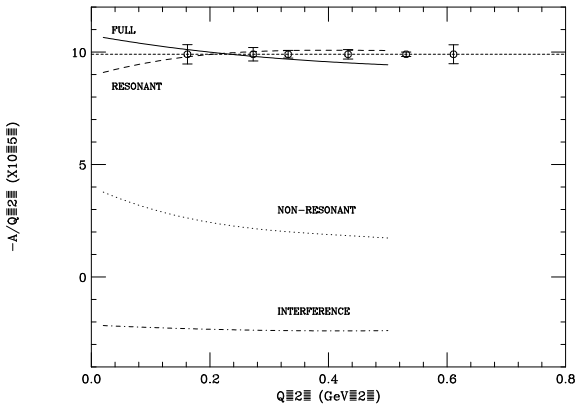

Figure 2: Asymmetries for the $\vec{e}+p$ inelastic reaction at the peak of the Δ resonance. The result of the full calculation (solid line) is compared to the contributions of the non-resonant background (dotted line), resonance (long dashed line), resonance neglecting the contribution from the axial form factor $G^A_{N\Delta}(Q^2)$ (short dashed line), and interference term (dot-dashed line). Included are the expected statistical uncertainties of our measurements in the several Q^2 bins of the reaction to be measured.

If one now includes the effects of the Siegert radiative correction, it is no longer possible to extract the axial contribution from the measured asymmetry, because it is not possible to subtract the unknown value of $A_{PV}^{N\Delta}(0)$ at $Q^2 = 0$. In this case, we can plot the asymmetry as a function of Q^2, and fit these data to the correct functional form given the parameterization of Adler where now two free parameters are allowed: the value of the asymmetry at $Q^2 = 0$ (the Siegert contribution) and the axial mass M_A. Shown in Fig. 4 is this fit, along with the resulting errors on the extracted parameters. As can be seen from the plot, using the G0 backward angle inelastic data alone, the uncertainty we could expect on the Siegert term is approximately 0.55 ppm, corresponding to $\delta d_\Delta \sim 14 g_\pi$, while the uncertainty on M_A increases by roughly a factor of 3 to ~ 0.97.

In order to constrain both of these quantities better, it is desirable to have measurements of the PV asymmetry in the $N \rightarrow \Delta$ transtion at very low Q^2 values. As part of the Q_{weak} program at Jefferson Lab, there are plans to spend some time measuring the parity violating asymmetry for inelastic electrons up to the peak of the Δ resonance, where a statistical precision of < 0.1 ppm is expected be achieved at a Q^2 value of 0.028 $(\mathrm{GeV/c})^2$. With such a low Q^2 data point, we examine the effect this would have on fitting the PV asymmetry in the $N \rightarrow \Delta$ transition allowing both the Siegert contribution and the axial form factor axial mass parameter to vary in the fit. For this study, we consider the Q_{weak} inelastic experimental scenario and conservatively assign a statistical error of 0.08 ppm on that data point. Plotted in Fig. 5 is

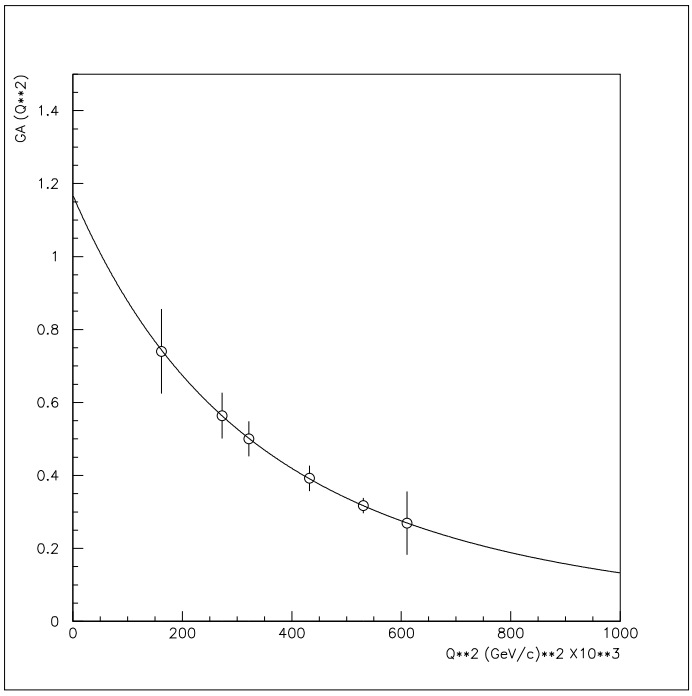

Figure 3: Axial vector transition form factor $G_{N\Delta}^{A}$ plotted vs. Q^2 assuming the Adler parameterization. Errors represent expected statistical errors only, and the allowed kinematical region for 2-π production has been excluded.

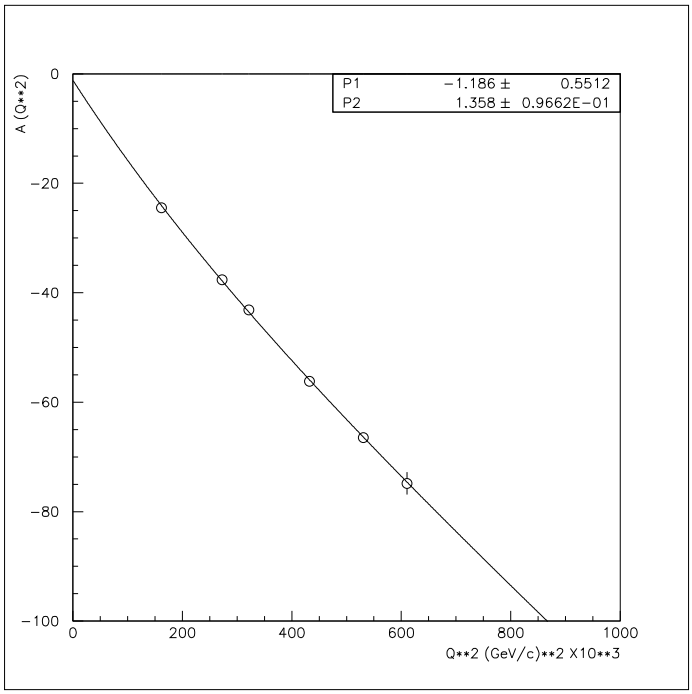

Figure 4: PV $N \to \Delta$ asymmetry plotted vs. Q^2. The fit uses the known functional form for the asymmetry including the Adler parameterization leaving the overall offset the asymmetry and the axial mass as free parameters. Here, $P1$ corresponds to the Siegert term, and $P2$ corresponds to M_A.

the result of this investigation, where we plot the expected PV asymmetries in the $N \to \Delta$ transition as a function of Q^2, along with the results of the fit. As can be seen from this final plot, the low Q^2 point significantly constrains the Siegert term (the value of $A_{PV}^{N\Delta}(0)$) to ~ 0.09 ppm (corresponding to $\sim 2.2 g_\pi$), while recovering good precision on the neutral weak axial mass parameter ($\delta M_A \sim 0.031$).

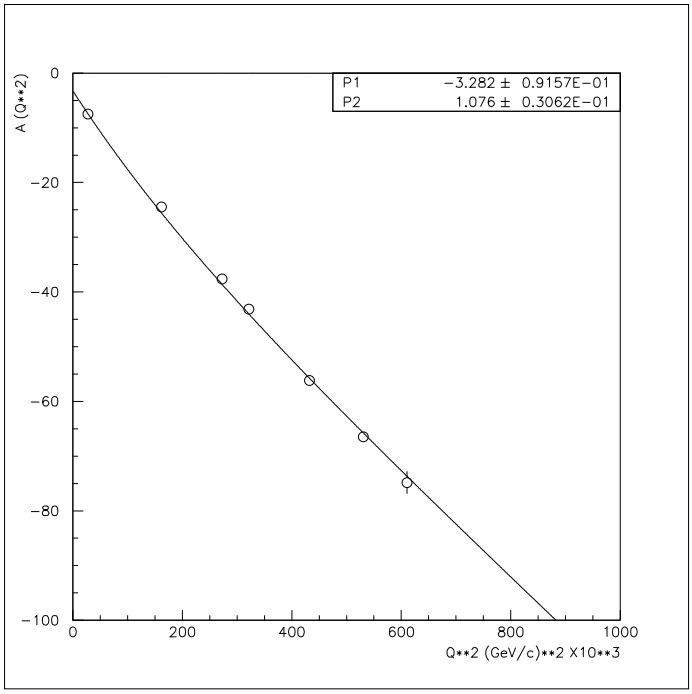

Figure 5: PV $N \to \Delta$ asymmetry plotted vs. Q^2 including a low Q^2 point obtainable using the Q_{weak} apparatus. The fit uses the known functional form for the asymmetry including the Adler parameterization leaving the overall offset the asymmetry and the axial mass as free parameters. Here, $P1$ corresponds to the Siegert term, and $P2$ corresponds to M_A.

3 Apparatus

Since the time of the original submission of the proposal for this experiment (E97-104), there has been significant progress in the development of the equipment required for the G0 backward angle measurements. In addition, all of the apparatus for the forward angle measurements has been completed, installed, debugged, and successfully used during two forward angle engineering runs, and in the forward angle production running. In this section, we present a brief summary of this progress, with particular emphasis on those subsystems which are required for backward angle running.

3.1 Detectors

The detector system to be used for these backward angle measurements consists of two arrays of scintillators for each of the eight G0 octants: a Focal Plane Detector (FPD) array (sixteen detectors per octant each viewed from two ends), which will also be used for the forward angle measurements, and a Cryostat Exit Detector (CED) array (nine detectors per octant each viewed from two ends). For backward angle electron detection, both arrays are required to determine the electron scattering angle and momentum, thereby providing an adequate separation between elastically and inelastically scattered electrons. In addition, to significantly reduce the contribution to both elastic and inelastic electron yields from π^-'s, a Čerenkov detctor using an aerogel based design will be positioned between the CED and FPD arrays. The FPD's have been successfully used for the forward angle running, so here we concentrate on the other two subsystems, the CED's and Čerenkov detectors.

3.1.1 CED's

The CED's are a critical component of the G0 backward angle running, and here we provide a summary of the progress to date on this detector package. In the original proposal, there were to be twelve individual CED's per octant, to be combined with the sixteen FPD's. Due to space constraints between the magnet end cap, beam line shielding, and the FPD octant support, three of the CED's closest to the beam line were eliminated from the design, leaving nine CED's per octant. Because these three CED's which were removed intercepted a large yield of lower momentum inelastically scattered electrons, our momentum transfer range does not reach as low as originally proposed, and our statistical uncertainty at lower momentum transfer is somewhat larger than originally expected. In addition, the lower momentum inelastically scattered electrons at each beam energy are no longer included, resulting in fewer Q^2 bins for the asymmetry measurement and axial transition form factor extraction.

The design of the remaining nine CED's has been completed, including the shapes of both the scintillators and light guides, and a procedure for manufacturing the correct shapes for the light guides has been developed and tested in the construction of a prototype CED. A detailed simulation of expected light yield from these detectors was performed, and the number of photoelectrons predicted was found to be more than adequate for these measurements. A prototype CED was constructed at TRIUMF, and tested at Louisiana Tech University using the same PMT/base assemblies to be used in the North American FPD's, and the amount of light collected was consistent with the predicted amount, i.e. more than adequate for these measurements [28, 29].

The construction of the CED's has been completed in the TRUIMF scintillator shop, and all CED's have been delivered to Jefferson Lab. All of the light guides have been cut, and the procedure for proper bending of the light guides has been finalized. All scintillators and light guides, manufactured at TRIUMF, are now at JLab, and assembly of the first octant has begun.

The design of the octant support structure for the CED's and Čerenkov detectors is complete. A secondary ferris wheel, as shown schematically in Fig. 6 will provide the support for both sets of detectors, and will be attached to the ferris wheel which supports the FPD's.

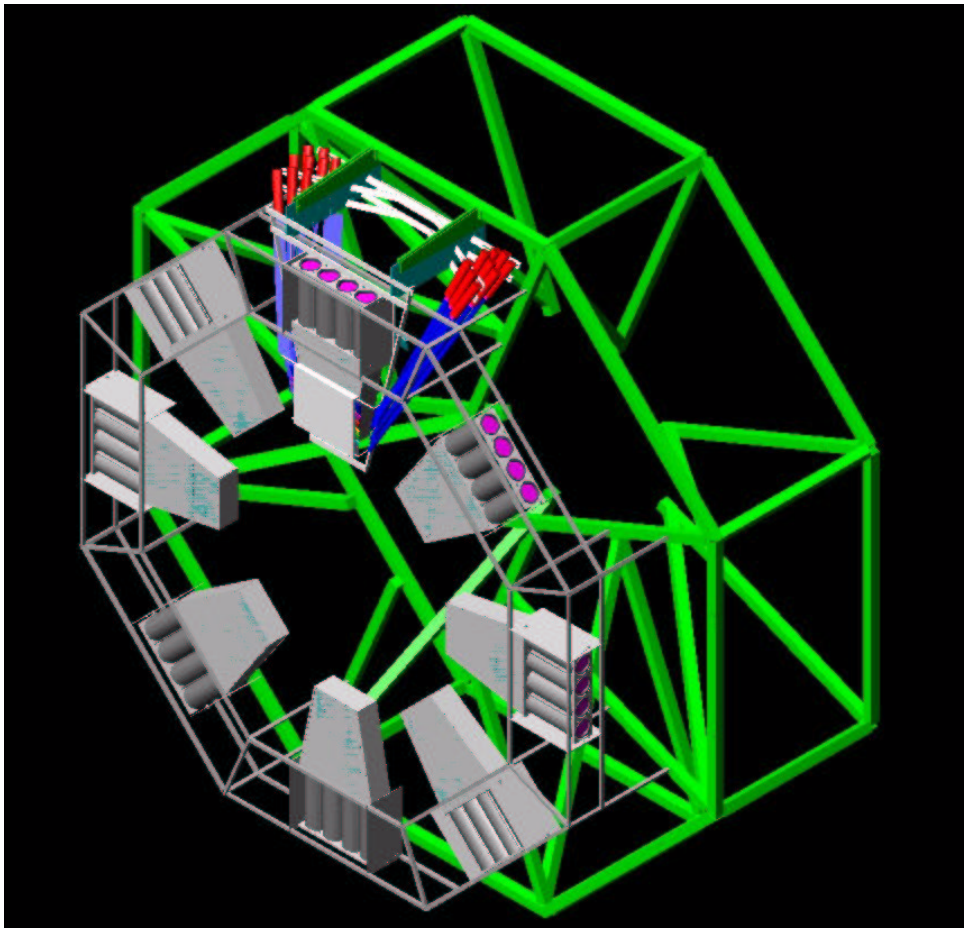

Figure 6: Concept of the full eight sectored G0 Phase II set up. The top sector shows both the CED and Čerenkov detector arrangement, while the other octants show the Čerenkov detectors only along with the ferris wheel support frame.

3.1.2 Čerenkov Detector

The π^- background from the $p(e^-,\pi^-)\pi^+ n$ reaction in the target and from $Al(e^-,\pi^-)X$ in the target endcaps will be significantly reduced with the use of particle identification between the electrons and π^-'s. Thus, this is the motivation to design an aerogel Čerenkov detector to provide excellent pion rejection across the full G0 momentum range, up to 400 MeV/c for $Q^2 = 0.5$ (GeV/c)^2. This, of necessity, must be an eight-sectored array of individual Čerenkov detectors mounted in conjuction with the CED-FPD sectors. This implies the construction of an extension to the detector supporting ferris wheel. The geometry of the aerogel Čerenkov detector is shown in Figure 6. A single octant detector is shown in more detail in Figure 7.

Negatively charged particles entering an octant of the G0 spectrometer pass through 5 cm of aerogel. The aerogel has an index of refraction $n = 1.03$, so that a particle with a speed such that $\beta \geq \frac{1}{1.03}$ will produce Čerenkov light. Thus, pions up to a momentum of 570 MeV/c will not produce any light. On the other hand, all primary electrons will produce light. Thus, the

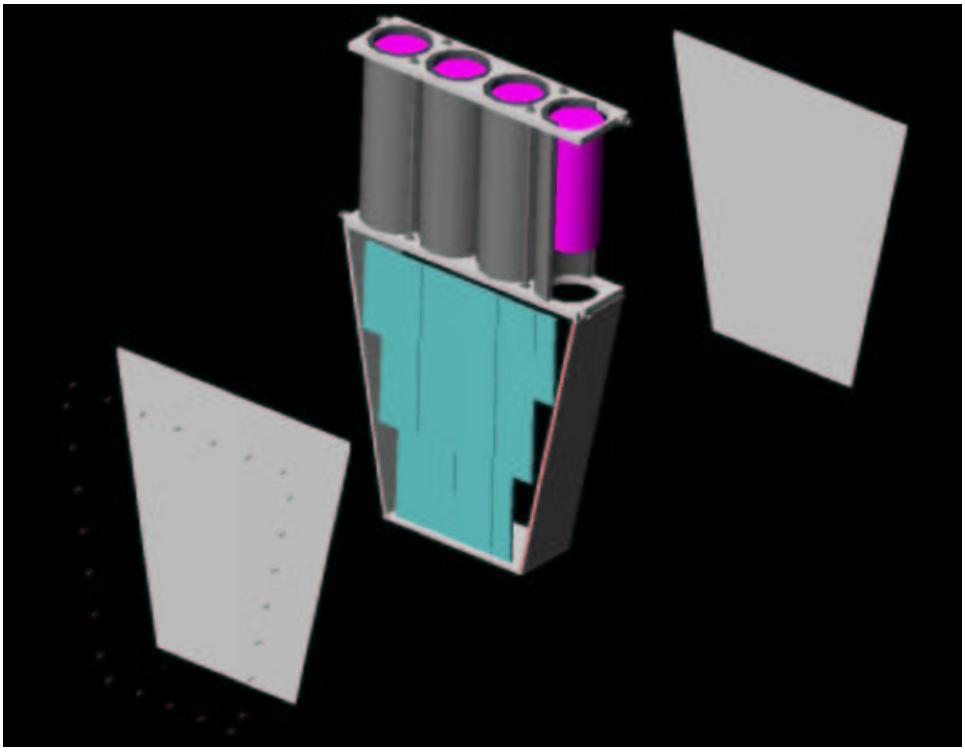

Figure 7: A view of the concept of a single octant light-box with aerogel Čerenkov radiator and PMT's.

detector will operate in *coincidence* mode and not in *veto* mode.

The light is emitted within a small angle ($\cos\theta_c = \frac{1}{1.03}$ at maximum) and enters a downstream region whose walls are lined with a white diffuse reflector. The likelihood of a photon reaching one of four phototubes is related to their active area compared to the total internal area of the light box, which is a little better than 4%. Other goals in the box design are to cover as large a fraction as possible of the G0 acceptance while keeping the timing spread as narrow as possible.

With 5 cm of clear aerogel, the electrons are expected to give about 6 photoelectrons; whereas a 400 MeV/c pion would have a rejection factor of $\frac{1}{125}$. This latter pion signal appears to arise mostly due to δ-rays produced in the CED's or elsewhere.

The phototubes for the Čerenkov counter for each octant will be tied together to produce one summed signal. This signal will be discriminated and sent to the backward angle coincidence electronics to be ANDed with the trigger. Using existing sampling techniques, Čerenkov ADC spectra could be used to check the calibration and pion rejection factor of each octant.

The typical time-width of the signal from an aerogel Čerenkov of this design is ~20 ns (due mainly to collection time in the light box), during which time the radiator is dead. This is because the light can bounce around in the box for some time. The rise time of the pulse is of the order of 1 ns. Beam pulses from JLab are delivered to the experiment every 32 ns.

Studies with both Monte Carlo simulation and a simple mock-up of the Čerenkov counter have been done. The various sub-groups have also constructed more realistic prototypes. Most of the assumptions above come from CIT tests and Grenoble and CIT simulations. At Caltech, a small Čerenkov test counter using a single phototube was built for the purpose of testing light yield and timing calculations from Monte Carlo simulations, and was found to produced results similar to the simulation. A first test detector was built at Caltech and tested at TRIUMF using a mixed particle test beam and the results indicate that the pion rejection is sufficient for our purposes. At TRIUMF a full size prototype was constructed and tested on the M11 $\beta \sim 1$ "electron" beamline. The French version of the detector is essentially identical, and similar test results have been obtained there.

All the parts for these detectors are either in-house (including Aerogel and phototubes) or are being manufactured. The French detectors will be shipped by the end of summer 2004, and the NA detectors will be assembled at JLab during the summer 2004.

3.2 Backward Angle Electronics

Since the original proposal for these measurements, the decision has been made that the four French octants will be instrumented using electronics developed at IPN-Orsay (DMCH-16X boards, based on flash-TDC and DSP technology), while the North American octants will be instrumented with the original Latching Time Digitizer (LTD) design. In both designs, much of the electronics used for forward-angle measurements will also be used for the backward-angle running. In particular, all of the PMT/base assemblies and associated power supplies used for the backing scintillator array for the FPD's will be used for the CED's, and all of the instrumentation for the backing array (e.g., analog splitters, constant fraction discriminators, mean timers, and ADC and TDC channels for the monitoring electronics) is also available for the CED array.

The philosophy of the backward-angle electronics design is based in large part on the fact that the electrons being detected ($E_{scattered} \geq 200$ MeV) are all moving with approximately the

same velocity, and therefore have a well defined flight time for each CED and each FPD. This is shown in Fig.'s 8 and 9, where we plot the flight time from the target to selected CED's and FPD's, respectively. Thus, a relatively tight time correlation can be made between a given CED and FPD pair and the arrival time of the beam at the LH_2 target. Consequently, the use of fast Programmable Logic Devices (PLD's) can provide hardware coincidences which can significantly reduce time uncorrelated backgrounds.

We have been able to use this relatively tight timing to make an important change to the front end of the electronics as compared with the original backward angle proposal. In order to take advantage of the more straightforward accelerator operation and the possibility of higher beam currents, the standard 499 MHz pulse structure will be adopted for the backward angle measurements. Therefore, instead of using our beam pickoff signal as the primary electronics trigger, the mean-timer ouputs of the CED's for a given octant will be ORed together and ANDed with the ORed outputs of the FPD's for the same octant. The maximum total rate per octant is 500 kHz (including elastic electrons, inelastic electrons, pions, and muons), and even with background rates in each CED and FPD of 500 kHz (maximum of background rates observed in the forward angle run), the random coincidence rate per octant is only about 500 kHz (assuming 20 ns gates). Therefore with a total maximum trigger rate of order 1 MHz, the deadtime at the the trigger level will be 2%. Commercial electronics will be used to generate these trigger signals.

The North American electronics chain for forward-angle measurements is shown schematically in Fig. 10. For the backward-angle measurements, the PMT's for the FPD backing detector array will be attached to the CED's, and the LTD's and "munger" redistribution boards will be replaced by custom logic circuitry developed at Louisiana Tech. Thus, the input to this new logic circuitry is the output of the mean timers for both the FPD's and CED's, a discriminated signal from the Čerenkov detector, and the trigger pulse described above. The output of this new circuitry is sent to the latching scalers to count the number of coincidences between detectors in the CED array and those in the FPD array.

Significant development on the coincidence logic circuitry for the North American octants has taken place since the time of the original proposal. The circuit design involves the use of PLD's mentioned above, programmed to implement all of the logic associated with the CED-FPD coincidences; the handling of "multiple hit" events (where more than one CED or more than one FPD fires on a given beam burst); and dead time monitoring. The logic signal from the Čerenkov detector, which signifies that it was in fact an electron which fired both the CED and FPD involved in the coincidence, will be used to enable a latch which allows the coincidence information to be sent to the scaler modules. Additional counting of CED and FPD singles rates, with various combinations of multiple hit logic and Čerenkov signals included, will be used for an estimate of the front end electronics dead time.

Enough of the PLD's have been obtained to construct all necessary prototype circuit boards; the programming software to burn these chips has been obtained, debugged, tested, and used for programming; and properties of the programmed PLD's as well as the logic contained in the programs have been tested. In the final configuration, a total of five boards will be needed per octant: one to handle the coincidence logic encoding; one to handle the multiple hit, Čerenkov, and dead time information; and three to handle TTL-ECL conversion to provide the appropriate level required by the latching scalers. All of the boards will be housed in a custom VME chassis which provides the necessary power and common ground to each. The custom VME chassis, in which four separate sets of five slot back planes (one for each NA octant) has been acquired

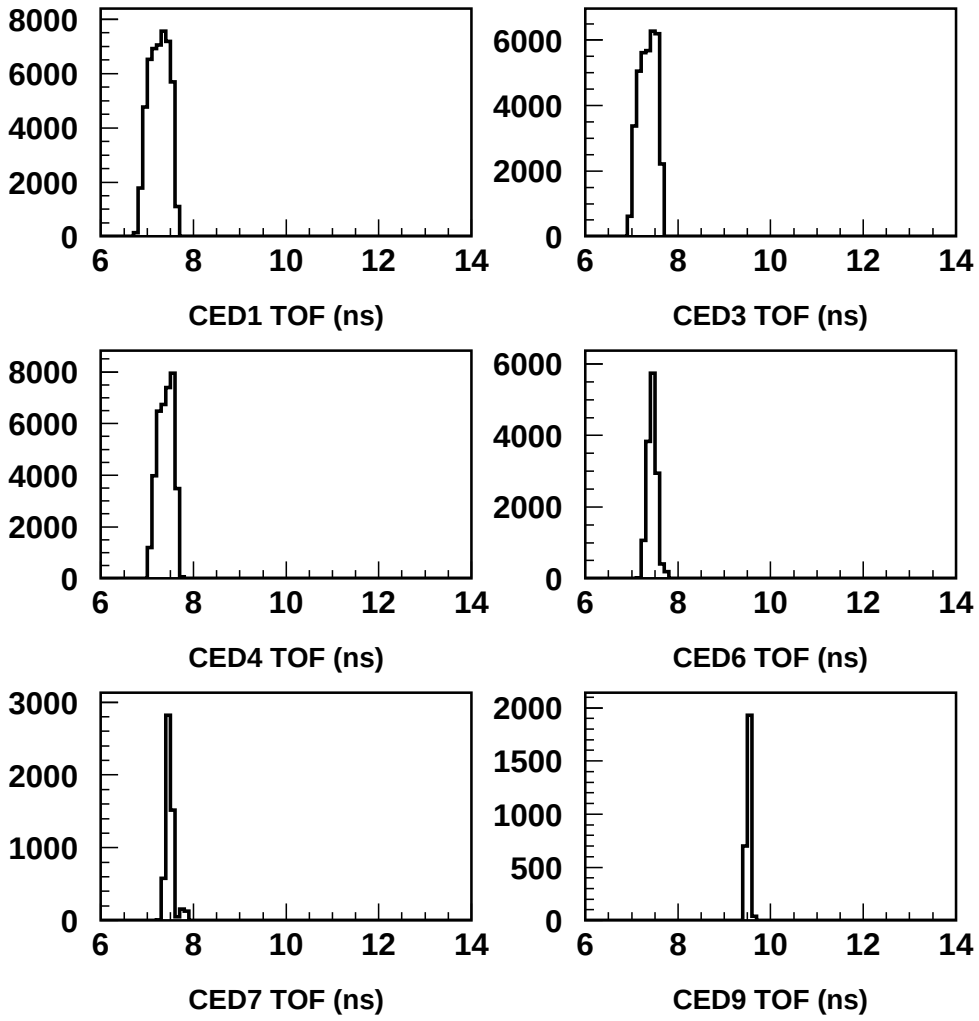

Figure 8: Flight times for electrons from the target to selected CED's.

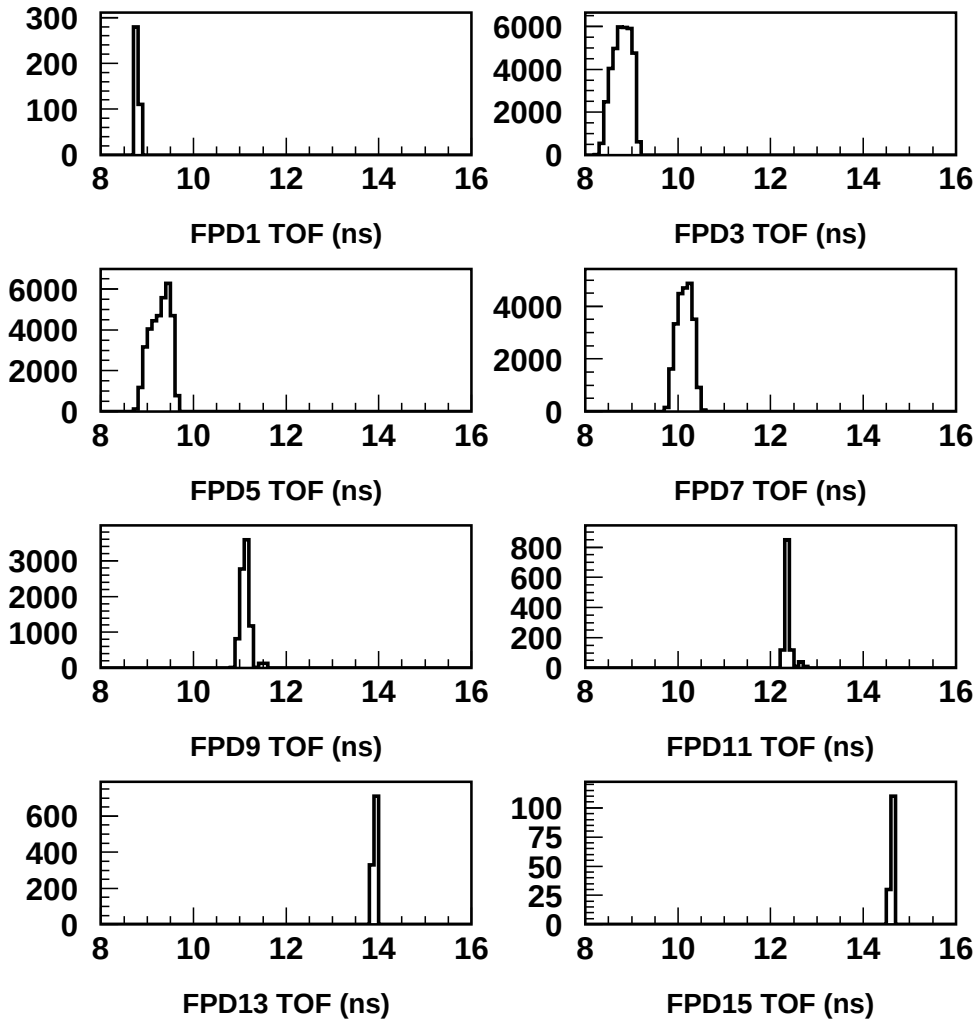

Figure 9: Flight times for electrons from the target to selected FPD's.

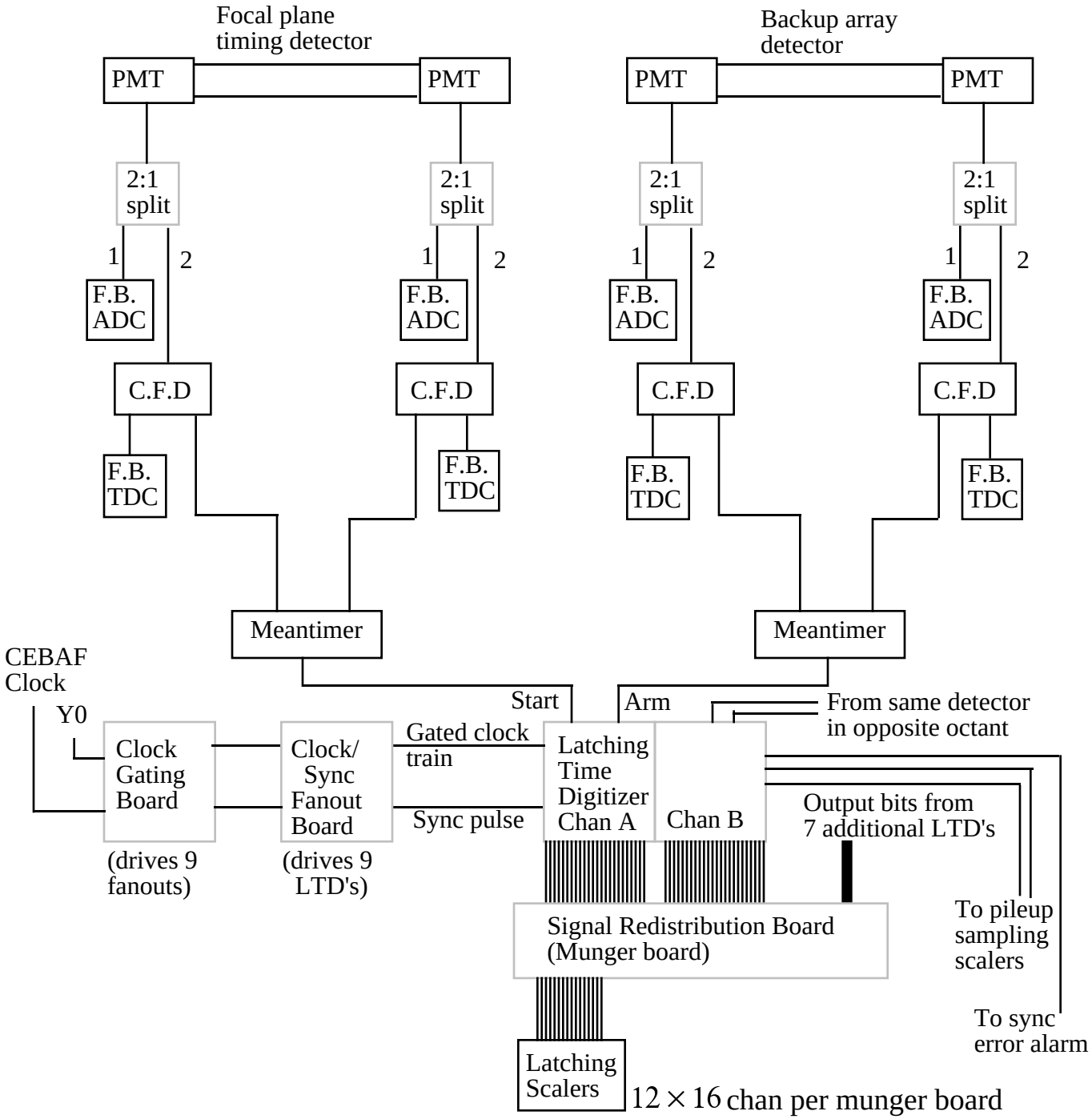

Figure 10: Electronics block diagram for the forward-angle running mode for the North American octants.

from a vendor. An entire set of five prototype boards to accommodate one octant has been manufactured and tested, and performs as designed. The output of these electronics has been sent to a spare 32 channel latching scaler, and read out with a CODA based acquisition system via a standard VME crate backplane. Tests have been performed on all logic sequences, multiple hit logic, as well as dead time effects. Synchronous trigger signals have been sent to the prototype electronics at rates up to 16 MHz, with zero dead time present. Tests involving random events in time, with a radioactive source firing scintillators to provide input to these electronics are underway. Additional programming for analysis of the data to be read during the experiment is currently underway. Manufacturing, stuffing, and testing of the final twenty circuit boards is expected to be completed by the end of 2004, and installation into the G0 electronics at Jefferson Lab is planned for early 2005.

Nearly identical logic and overall philosophy will be used for the French electronics. For one octant, the front end instrumentation (discrimination and meantiming) will be handled by two DMCH-16X boards. The meantimed outputs, available on the front panel, will be sent to a CED-FPD coincidence module.

The coincidence board, develped by ISN Grenoble, contains all Programmable Logic Devices and scalers needed for the counting of individual coincidences between each CED and each FPD. As in the North American design, the CED-FPD coincidences will be allowed during a short time window ($\sim$ 8 ns) to generate the trigger, and the Čerenkov counter will provide an enable signal for the counting. Also as in the North American design, additional counting associated with the singles rates in the CED's and FPD's will be used for the estimate of the number of multiple hit events and for deadtime monitoring. In addition to the singles counting available in the coincidence board, the DMCH-16X modules also provide the time of flight information for the individual CED's and FPD's, which can be used for an accurate estimate of the number of lost events due to the deadtime of the front end electronics.

One CED-FPD coincidence module will be able to handle two octants. For the four french octants, the VXI crate will therefore support eight DMCH-16X and two CED-FPD coincidence modules. A prototype of the CED-FPD coincidence module has been completed, and tests are underway.

3.3 Data Acquisition

The data acquisition requirements for the backward-angle running configuration are almost identical to those for forward-angle running. Only small differences in the data stream will be present for both the North American and French octants. The data acquisition has been thoroughly tested and successfully used during the G0 forward angle running. Rather than having outputs of the LTD's connected to the 32 bit latching scalers as was done for the forward angle measurements, the outputs of the coincidence electronics will be used as input to the scalers. The data acquisition structure will be identical for the backward angle running as it was during the forward angle running.

4 Kinematics and Cross Section Calculation

The design of the $N \rightarrow \Delta$ transition experiment in this proposal has several constraints which have already been taken into account. The G0 spectrometer and associated collimator design

is optimized for elastic forward proton and backward electron scattering, and will be used for the $N \rightarrow \Delta$ transition asymmetry measurements with no modification. For these inelastic asymmetry measurements made during the same running period that the elastic electron-proton asymmetry measurements are made, we can not alter any of the G0 spectrometer settings.

The asymmetry in the $N \rightarrow \Delta$ channel will be measured with the G0 spectrometer in the backward angle measurement mode. In this configuration, elastically scattered electrons are detected in an angular range centered around $\theta_e \sim 110^\circ$. Using the magnetic field setting, target position and target length for the elastic channel settings, we can calculate the kinematical limits for the inelastic electrons, which are shown in Table 1.

The measurement of the $N \rightarrow \Delta$ asymmetry using the G0 spectrometer is an inclusive measurement, in which only inelastically scattered electrons are detected. The calculation of the cross section in this kinematical range is based partially on the work of J. W. Lightbody and J.S. O'Connell [30] and F.W. Brasse *et al.* [31, 32]. The inelastic electron scattering cross section is calculated as the product of the virtual photon flux and the total cross section for virtual photon-proton scattering, as a function of Q^2 of the virtual photon and the invariant mass of the photon-proton system. The calculation of the total cross section for virtual photon-proton scattering is based on the parametrization by Brasse *et al.* [31, 32]. The results for some electron angles are shown in Fig. 11 for an electron beam momentum of E=0.585 GeV.

$E(GeV)$	$Q^2_{el.}((GeV/c)^2)$	$Q^2_{inel.}((GeV/c)^2)$	$E'_{inel.}$ (GeV)	$\theta'_{inel.}(deg)$
0.424	0.3	0.04 - 0.22	0.060 - 0.190	90 - 105
0.585	0.5	0.10 - 0.40	0.070 - 0.270	90 - 110
0.799	0.8	0.20 - 0.65	0.100 - 0.315	90 - 120

Table 1: Inelastic kinematics for magnetic fields optimized for the elastic channel, calculated for three beam energies.

The calculation of the Δ electroproduction cross section for the beam energies below 1 GeV is in good agreement with the existing data [30], and can be used to estimate the rates and uncertainties for the $N \rightarrow \Delta$ asymmetry measurements.

5 Rates

The rates for the inelastically scattered electrons are calculated as:

$$Rates = \int_{E'_{min}}^{E'_{max}} \int_{\Delta\Omega} \frac{d\sigma}{dE' d\Omega} dE' d\Omega \tag{8}$$

where $\frac{d\sigma}{dE' d\Omega}$ is the double differential inelastic electron cross section, E'_{min} and E'_{max} are the lower and upper limits of the detected electron momentum, and $\Delta\Omega$ is the covered solid angle. For the inelastic channel, the scattered electron momentum range $\Delta E'$ and solid angle $\Delta\Omega$ are small enough in each Focal Plane Detector-Cryostat Exit Detector coincidence measurement to allow Eq.(1) to be replaced by:

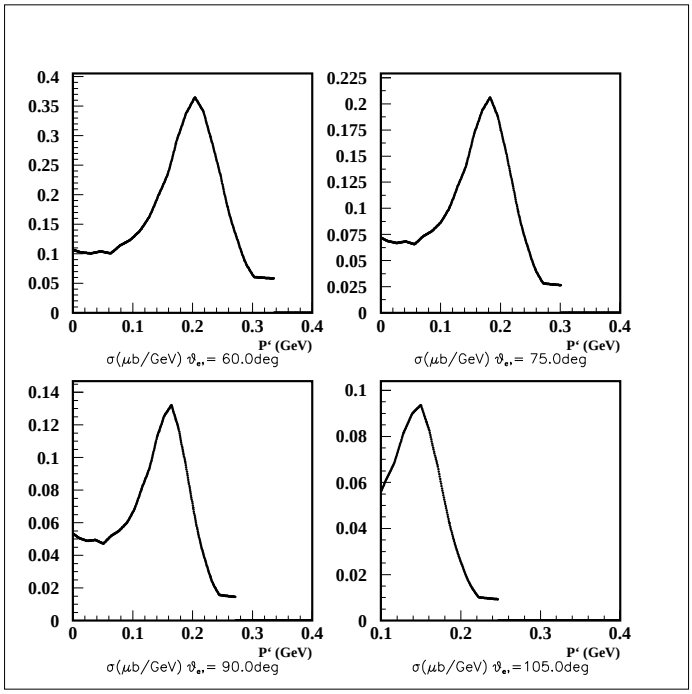

Figure 11: Inelastic electron-proton cross section calculations for E=0.585 GeV, at four electron scattering angles.

$$Rates = \overline{\frac{d\sigma}{dE' d\Omega}}\ \Delta E'\ \Delta\Omega, \tag{9}$$

where $\overline{\frac{d\sigma}{dE' d\Omega}}$ is the average inelastic electron cross section for electrons having a momentum range $\Delta E'$ detected in the solid angle $\Delta\Omega$.

The measurement of the $N \rightarrow \Delta$ channel in these measurements is broken into many of $\Delta\Omega$ and $\Delta E'$ bins, depending on the number of Focal Plane Detectors and Cryostat Exit Detectors used in the experiment. The analysis of rates is done by assuming coincidences between 9 Cryostat Exit Detectors and 16 Focal Plane Detectors. The total number of possible FPD-CED coincidence combinations is 144, but due to the allowed phase space for single pion production, only a portion of these are used for the $N \rightarrow \Delta$ measurement.

The procedure for the rate calculation can be divided into several steps:

- for the single pion production reaction, the phase space density of the three particle final states is calculated numerically using the CERN library routine GENBOD [33]
- the inelastically scattered electrons are tracked through the G0 spectrometer in the G0 Geant simulation program
- the electron momentum range and solid angle are calculated from the Monte Carlo simulation by requiring that the electrons generated in the target track through a particular Cryostat Exit Window Detector segment and particular Focal Plane Detector segment
- beam current, target length and thickness, and luminosity are assumed to be the same as for the elastic scattering experiment [34], and are represented in Table 2.

Average current:	80 μA
Target length:	20 cm
Luminosity:	$4.2 \times 10^{38}\ cm^{-2} s^{-1}$

Table 2: Beam and target parameters for luminosity determination.

Some results from the procedure described can be seen for a beam energy E=0.585 GeV in Figure 12, where the scattered electron momentum and angle are shown for the Δ resonance in the space of Focal Plane Detector-Cryostat Exit Detector coincidences.

Finally, calculated Q^2 values and rates in the FPD-CED space for the same beam energy E=0.585 GeV are shown in Fig. 13.

6 Statistical Uncertainties of the Measured Asymmetries

In the previous two sections, we have described a procedure for calculating inelastically scattered electron kinematics, cross section and counting rates for particular CED segment-FPD segment coincidences. The asymmetry is then determined from yields for the two beam helicities (each measured for a time T_h) as [34]:

$$A^{meas} = \frac{Y_+ - Y_-}{Y_+ + Y_-}, \tag{10}$$

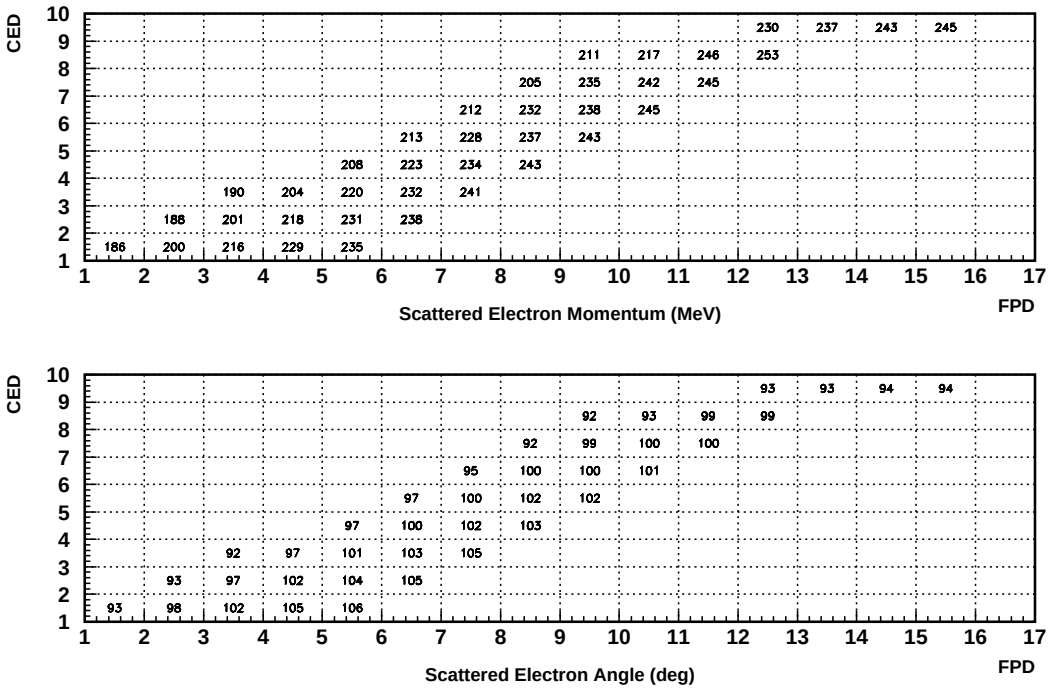

Figure 12: Scattered electron momentum (top) and scattering angle (bottom) in FPD-CED space for E=0.585 GeV. As an example, the distribution of coincidences between CED number 3 and FPD number 4 has a mean momentum of 204 MeV/c.

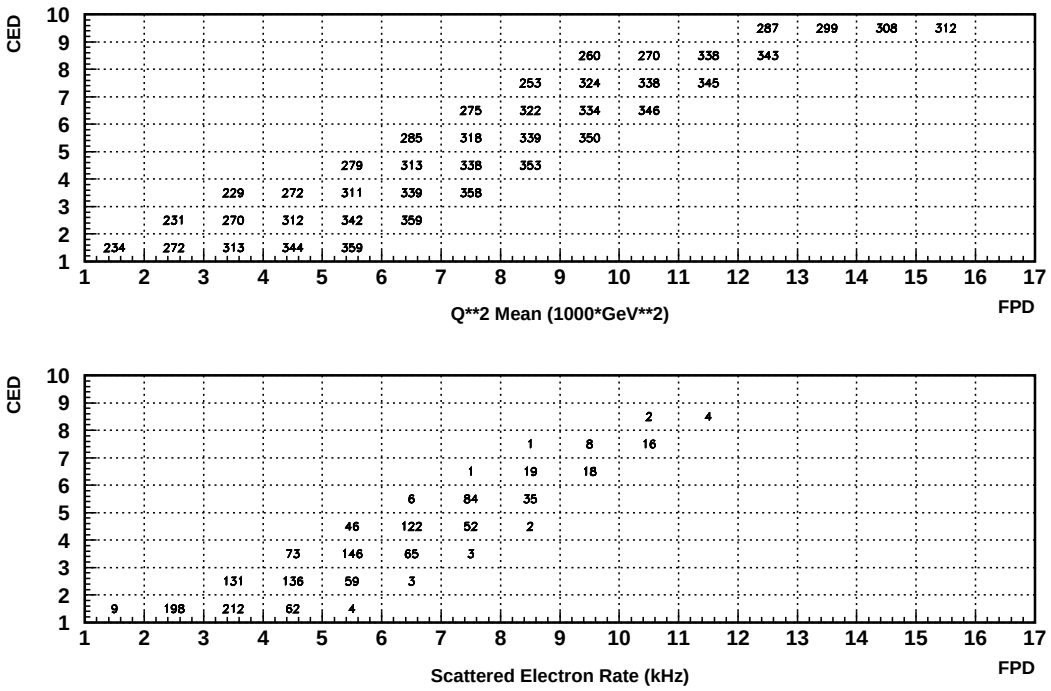

Figure 13: Scattered electron Q^2 value (top) and rates (bottom) in FPD-CED space for E=0.585 GeV.

where

$$Y_h = \frac{Rate \times T_h}{Q_h} = \frac{N_h}{Q_h}, \tag{11}$$

and N_h and Q_h are the total number of counts in the detectors and the beam charge passing through the target in time T_h, respectively.

The number of counts in the detectors for the two beam helicities is approximately equal, $N_+ \simeq N_- = N/2$, where N is the total number of counts. Neglecting, for now, any dilution factor, the statistical uncertainty we expect to achieve is simply:

$$\Delta A^{meas} = \frac{1}{\sqrt{N}}. \tag{12}$$

While a detailed description of the $N \rightarrow \Delta$ transition asymmetry is given in previous sections and the appendices, to calculate the statistical precision of the proposed measurement, we use only the dominant leading term in the asymmetry,

$$A = \frac{G_F}{\sqrt{2}} \frac{Q^2}{2\pi\alpha} \tilde{\alpha}, \tag{13}$$

where Q^2 is the four momentum transfer squared, $G_F = 1.17 \times 10^{-5}(\mathrm{GeV}^{-2})$ is the Fermi coupling constant, $\alpha = 1/137.04$ is the electromagnetic coupling constant, and $\tilde{\alpha}$ is taken to be -0.5756 (with the standard model value of $\sin^2\theta_W = 0.2122$).

7 Background Consideration

In the presence of background, the measured asymmetry A_m is related to the inelastic asymmetry A_i by the following expression [34]:

$$A_m = \frac{A_i R_i + A_b R_b}{R_i + R_b} \tag{14}$$

where R_i and R_b (A_i and A_b) are the total counting rates (asymmetries) for the inelastic and the background events, respectively.

The magnetic analysis of the G0 spectrometer and collimator system ensures that only negatively charged particles scattered from the target will reach both sets of detectors. For extraction of the axial transition form factor $G^A_{N\Delta}(Q^2)$, we have limited our acceptance for electrons out to the region where inelastically scattered electrons which have created two pions in the target are detected. There can be, however, π^-'s from the target which can be accepted into this region. These π^-'s originate from two sources: from the $ep \rightarrow ep\pi^+\pi^-$ reaction in the hydrogen target, and from single π^- production on the neutrons in the aluminum target end caps.

For measurements on hydrogen, which is the focus of this proposal, we can make estimates of the amount of contamination from π^-'s using the same programs written by Lightbody and O'Connell [30], which we used to estimate the electron rates, as well as MAID2000, a program which calculates pion photo and electroproduction on the nucleon. We found that both programs produce similar rates which are in agreement with the results of π^- cross section measurements performed in Hall C [35], where both electrons and π^-'s were detected at an angle of $\theta = 136.5^\circ$ for beam electrons of 824 MeV incident on a LH_2 target.

Our pion rate estimates, an example of which we present in Fig. 14 in CED-FPD space for the $ep \to ep\pi^+\pi^-$ reaction for an incident beam energy of 585 MeV, shows a significant, $\sim 100\%$ π^- contamination to the $N \to \Delta$ yields. At the lowest beam energy studied (424 MeV), the π^- contamination is negligible, but increases with increasing beam energy. For a beam energy of 585 MeV, the π^- contamination is $\sim 100\%$ as shown in Fig. 12, and increases up to $\sim 400\%$ for a beam energy of 799 MeV. The π^- rate from single π^- production on the neutrons in the aluminum target end caps has also been estimated from the Lightbody/O'Connell code, and was found to be an order of magnitude smaller than the rate from the $ep \to ep\pi^+\pi^-$ reaction, with similar angular dependence. For the quasielastic measurements on deuterium to be performed in the G0 physics program, the π^- contamination to both the elastic and inelastic channels is more severe due to single π^- production on the neutrons in deuterium. Additionally, there have been no measurements and no theoretical estimates on the size of the asymmetry in the $p(\vec{e}^-, \pi^-)X$ and $d(\vec{e}^-, \pi^-)X$ reactions, so that corrections to the elastic and $N \to \Delta$ asymmetries due to these π^-'s would not be possible. Instead, we will use particle identification to hardware reject the large number of π^-'s expected from the target, and this is the function of the Čerenkov detector discussed above.

Another source of background in the inelastic channel is due to the finite size of both the CED's and FPD's. Although the coincidences between the CED's and FPD's provide a determination of scattered electron momentum and angle, there are certain CED-FPD combinations in which both elastically and inelastically scattered electrons contribute. This results in a small contamination of the elastic yield due to inelastic electrons, and a small contamination of the inelastic yield due to elastic electrons, both of which increase with increasing beam energy. Fortunately, the parity violating asymmetries in both of these reactions will be measured *simultaneously* in CED-FPD combinations not in the overlap region, allowing for a correction to each of these asymmetries due to the contamination of the other reaction. Using the rate estimates described in the previous sections, we find that the resulting increase in statistical error on the inelastic asymmetry due to elastic contamination is less than 0.1 ppm in any Q^2 bin studied, and is therefore negligible compared with the overall statistical error in each Q^2 bin.

Finally, due to the finite length of the LH_2 target, the incident beam electrons can lose energy (radiating bremsstrahlung photons) before scattering from a target proton. There will therefore be an elastic "radiative tail" which will contaminate the inelastic measurement. The yield for the elastic "radiative tail" underneath the Δ resonance can be estimated by knowing how the cross sections for bremsstrahlung and elastic scattering depend on electron and photon energy [36]. Because these measurements will be performed with different beam energies, different amounts of the elastic radiative tail will contribute, depending on which beam energy is used. In the worst case, corresponding to the lowest beam energy, we estimate that the yield from this contamination is of order 1% of the inelastic pion production yield. Also, as just discussed, the elastic parity violating asymmetry will simultaneously be measured, allowing us to calculate the contribution to the inelastic asymmetry from this background process. Thus, we conclude that the contribution from the elastic radiative tail to the asymmetry in the inelastic channel is small, and easily correctable.

8 Summary and Requested Beam Time and Support

We are requesting no additional beam time for these measurements, but only for the parity violating $N \to \Delta$ measurements to continue to be recognized as an officially approved TJNAF

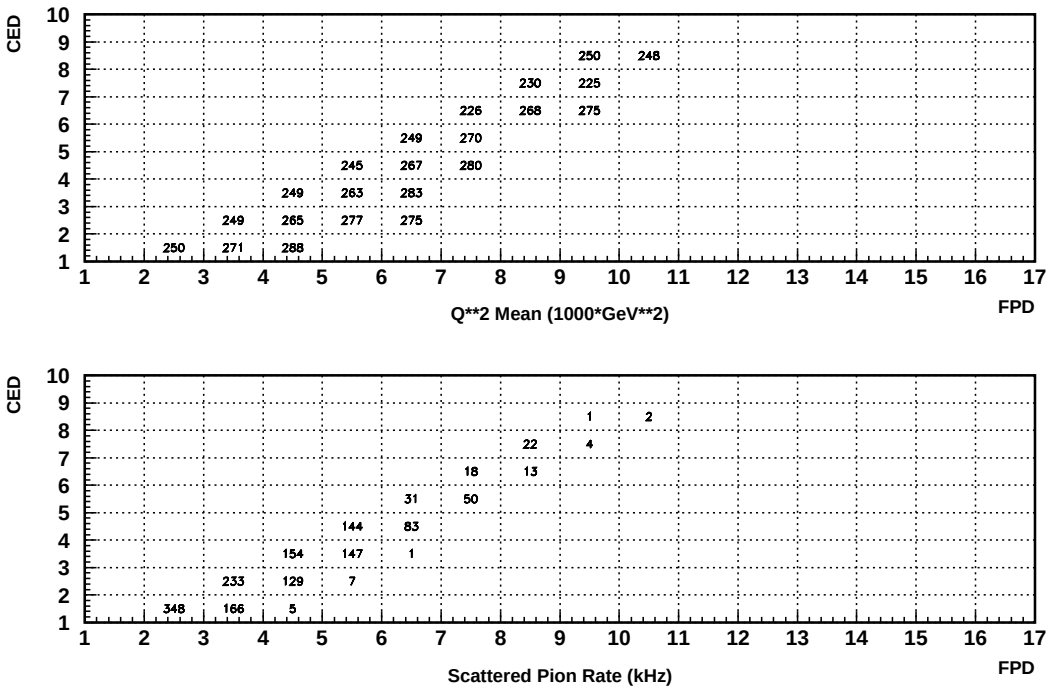

Figure 14: Pion Q^2 values (top) and counting rates (bottom) in FPD-CED space for E=0.585 GeV.

experiment. The measurements described throughout this proposal will be made during the same running period as the G0 experiment in the backward angle mode. In addition, all beam, hardware, electronics, and data acquisition requirements for the G0 backward angle elastic measurements are sufficient to complete the inelastic measurements. Coincidences between the Focal Plane and Cryostat Exit Detectors discussed throughout this proposal are necessary to identify independently the elastic and inelastic channels during the G0 backward angle measurements, and allow the parity violating asymmetry to be mapped out across the Δ resonance simultaneously. These measurements provide direct access to the axial transition form factor $G_{N\Delta}^{A}$, the Q^2 dependence of which we will be able to map out in the range $0.1 \leq Q^2 \leq 0.6$ (GeV/c)^2, and represent the first determination of this form factor in the neutral current sector of the weak interaction.

A Details of the Asymmetry

In this appendix, we relate the notation used here to notations used by other authors [9, 2], and show the explicit kinematic dependences of the coefficients of the electromagnetic and weak transition form factors.

In the notation of Ref. [2], the asymmetry, containing only resonant terms, is written

$$A_{RL} = -\frac{2Q^2}{e^2(Q^2+M_Z^2)}\{\alpha g_{A,e} + \beta g_{V,e}\frac{2(E+E')}{M}\frac{W_3 \sin^2\frac{\theta_e}{2}}{2W_1^{EM}\sin^2\frac{\theta_e}{2} + W_2^{EM}\cos^2\frac{\theta_e}{2}}\}, \tag{15}$$

where $g_{V,e}$ and $g_{A,e}$, are given, in the minimal SU(2)$_L$×U(1) model, by [2]

$$g_{V,e} = \frac{-e}{4\sin\theta_W\cos\theta_W}(1-4\sin^2\theta_W)$$

and

$$g_{A,e} = \frac{e}{4\sin\theta_W\cos\theta_W},$$

where e is the electron charge, and $\sin^2\theta_W$ is the weak mixing angle, α and β are given by [2]

$$\alpha = \frac{e}{2\sin\theta_W\cos\theta_W}(1-2\sin^2\theta_W),$$

$$\beta = -\frac{e}{2\sin\theta_w\cos\theta_W},$$

the structure functions are given by [2]

$$\begin{aligned}
W_1^{EM} &= \frac{c}{6M^4}\{a^2[D_3(Q^2)]^2 + b^2[D_4(Q^2)]^2 + abD_3(Q^2)D_4(Q^2)\},\\
W_2^{EM} &= \frac{2Q^2}{3M^2}\{a[D_3(Q^2)]^2 + c[D_4(Q^2)]^2 + bD_3(Q^2)D_4(Q^2)\},\\
W_3 &= \frac{1}{3M^2}[2aD_3(Q^2)+bD_4(Q^2)]\{(b-2c)\frac{M}{2M'}C_3^A(Q^2) + \frac{b}{2}C_4^A(Q^2) - M^2C_5^A(Q^2)\},
\end{aligned} \tag{16}$$

with

$$\begin{aligned} a &= (M+M')^2+Q^2, \\ b &= (M+M')(M-M')+Q^2, \\ c &= (M-M')^2+Q^2, \end{aligned} \tag{17}$$

and

$$\begin{aligned} D_3(Q^2) &= -\frac{M}{M'}C_3^\gamma(Q^2), \\ D_4(Q^2) &= \frac{M}{M'}C_3^\gamma(Q^2)+C_4^\gamma(Q^2). \end{aligned} \tag{18}$$

To convert coupling strengths, consider only the first term, and assume $Q^2 \ll M_Z^2$. Then,

$$\begin{aligned} A_{RL} &= -\frac{2Q^2}{e^2M_Z^2}\alpha g_{A,e} \\ &= -\frac{2Q^2}{e^2M_Z^2}\left(\frac{e}{2\sin\theta_W\cos\theta_W}\right)\left(\frac{e}{4\sin\theta_W\cos\theta_W}\right)(1-2\sin^2\theta_W) \\ &= \frac{2Q^2}{M_Z^2}\frac{1}{8\sin^2\theta_W\cos^2\theta_W}[-(1-2\sin^2\theta_W)]. \end{aligned}$$

Now, we use [9]

$$M_W^2 = M_Z^2\cos^2\theta_W,$$

to get

$$A_{RL} = \frac{2Q^2}{8M_W^2\sin^2\theta_W}[-(1-2\sin^2\theta_W)].$$

Next, we use [9]

$$\frac{G_F}{\sqrt{2}} = \frac{g^2}{8M_W^2}$$

and

$$e = g\sin\theta_W$$

to obtain

$$A_{RL} = \frac{2Q^2}{e^2}\frac{G_F}{\sqrt{2}}[-(1-2\sin^2\theta_W)].$$

Finally, we use

$$e^2 = 4\pi\alpha$$

to get

$$\begin{aligned} A_{RL} &= \frac{G_F}{\sqrt{2}}\frac{Q^2}{2\pi\alpha}[-(1-2\sin^2\theta_W)] \\ &= \frac{G_F}{\sqrt{2}}\frac{Q^2}{2\pi\alpha}\tilde{\alpha}. \end{aligned}$$

Similarly,

$$-\frac{2Q^2}{e^2M_Z^2}\beta g_{V,e} = \frac{G_F}{\sqrt{2}}\frac{Q^2}{2\pi\alpha}\tilde{\beta}.$$

We now have

$$A_{RL} = \frac{G_F}{\sqrt{2}}\frac{Q^2}{2\pi\alpha}\{\tilde{\alpha}+\tilde{\beta}\frac{(2\tan^2\frac{\theta_e}{2})W_3}{(2\tan^2\frac{\theta_e}{2})W_1^{EM}+W_2^{EM}}\}, \tag{19}$$

where W_1^{EM}, W_2^{EM}, and W_3 are given by Eq. (16) above, and we have divided both numerator and denominator of Eq. (15) by $\cos^2\frac{\theta_e}{2}$ (we note that no measurements will be made at θ_e=180°). Carrying through some algebra yields

$$\begin{aligned} (2\tan^2\frac{\theta_e}{2})W_1^{EM}+W_2^{EM} = {} & h_{33}(Q^2,\theta_e)[C_3^\gamma(Q^2)]^2+h_{34}(Q^2,\theta_e)C_3^\gamma(Q^2)C_4^\gamma(Q^2) \\ & +h_{44}(Q^2,\theta_e)[C_4^\gamma(Q^2)]^2, \end{aligned} \tag{20}$$

where

$$\begin{aligned} h_{33}(Q^2,\theta_e) &= \frac{1}{3M'^2}[(a^2+b^2-ab)c\frac{\tan^2\frac{\theta_e}{2}}{M^2}+2(a+c-b)Q^2], \\ h_{34}(Q^2,\theta_e) &= \frac{1}{3MM'}[(2b^2-ab)c\frac{\tan^2\frac{\theta_e}{2}}{M^2}+2(2c-b)Q^2], \\ h_{44}(Q^2,\theta_e) &= \frac{1}{3M^2}[b^2c\frac{\tan^2\frac{\theta_e}{2}}{M^2}+2cQ^2], \end{aligned} \tag{21}$$

with a, b, and c defined in Eq. (17).

Similarly,

$$\begin{aligned} (2\tan^2\frac{\theta_e}{2})W_3 = {} & [h_3(Q^2,\theta_e)C_3^\gamma(Q^2)+h_4(Q^2,\theta_e)C_4^\gamma(Q^2)]\times \\ & [g_3(Q^2)C_3^A(Q^2)+g_4(Q^2)C_4^A(Q^2)+g_5(Q^2)C_5^A(Q^2)], \end{aligned} \tag{22}$$

where

$$\begin{aligned} h_3(Q^2,\theta_e) &= \frac{2M}{3M'}(b-2a)\frac{\tan^2\frac{\theta_e}{2}}{M^2}, \\ h_4(Q^2,\theta_e) &= \frac{2}{3}b\frac{\tan^2\frac{\theta_e}{2}}{M^2}, \\ g_3(Q^2) &= \frac{M}{2M'}(b-2c), \\ g_4(Q^2) &= \frac{b}{2}, \\ g_5(Q^2) &= -M^2. \end{aligned} \tag{23}$$

Substituting Eq.'s (20) and (22) into Eq. (19) yields

$$A_{RL} = \frac{G_F}{\sqrt{2}}\frac{Q^2}{2\pi\alpha}[\tilde{\alpha} + \tilde{\beta}F(Q^2, E, E', \theta_e)], \tag{24}$$

where

$$F(Q^2, E, E', \theta_e) = \frac{(E+E')}{M}H^{EM}(Q^2, \theta_e)G^A_{N\Delta}(Q^2), \tag{25}$$

with

$$H^{EM}(Q^2, \theta_e) = \frac{h_3(Q^2, \theta_e)C_3^\gamma(Q^2) + h_4(Q^2, \theta_e)C_4^\gamma(Q^2)}{h_{33}(Q^2, \theta_e)[C_3^\gamma(Q^2)]^2 + h_{34}(Q^2, \theta_e)C_3^\gamma(Q^2)C_4^\gamma(Q^2) + h_{44}(Q^2, \theta_e)[C_4^\gamma(Q^2)]^2}, \tag{26}$$

and

$$G^A_{N\Delta}(Q^2) = g_3(Q^2)C_3^A(Q^2) + g_4(Q^2)C_4^A(Q^2) + g_5(Q^2)C_5^A(Q^2). \tag{27}$$

We note here that, in full generality, $C_6^A(Q^2)$ would contribute (see Eq. (3)), but enters into this part of the asymmetry with a factor of $\frac{m_e}{M}$ and is therefore neglected [2]. Additionally, the form of $H^{EM}(Q^2, \theta_i)$ depends on the assumption that $C_5^\gamma(Q^2) = 0$. The physics justification for this assumption is two-fold: a) the theory of the spin-$\frac{3}{2}$ field requires that $C_4^\gamma(Q^2) = C_5^\gamma(Q^2) = 0$, and b) the single pion photoproduction and electroproduction data can be adequately described with $C_4^\gamma(Q^2) = C_5^\gamma(Q^2) = 0$, or $C_5^\gamma(Q^2) = 0$ and $C_4^\gamma(Q^2) = -\frac{M}{M+M'}C_3^\gamma(Q^2)$ [2].

B Discussion of Non-Resonant Background

As discussed throughout this proposal, the yield for single pion electroproduction from the proton is dominated by the $N \to \Delta$ resonance, but there are non-resonant processes which contribute. While estimates have been given as to the contribution these processes make to the parity violating asymmetry, the non-resonant background must be understood for a proper interpretation of the data to be obtained from these proposed measurements. To bring out the main features of the parity violating asymmetry in inclusive π electroproduction in the Δ resonance region, an analysis of the asymmetry obtained from the incoherent summation of the coincident $p\pi^0$ and $n\pi^+$ charge states (*i.e.*, the decay of the Δ^+) has been performed [5, 37]. They find

$$A^\pi_{RL} = -\frac{1}{2}\frac{G_F}{\sqrt{2}}\frac{Q^2}{2\pi\alpha}(\Delta^\pi_{(1)} + \Delta^\pi_{(2)} + \Delta^\pi_{(3)}), \tag{28}$$

where $\Delta^\pi_{(1)}$ corresponds to the axial vector electron-vector quark isovector resonant contribution, $\Delta^\pi_{(2)}$ gives the axial vector electron-vector quark non-resonant background contributions (both isovector and isoscalar), and $\Delta^\pi_{(3)}$ gives the vector electron-axial vector quark contribution (both resonant isovector and non-resonant isoscalar). These terms are given explicitly by

$$\begin{aligned}
\Delta^\pi_{(1)} &= g_A^e \xi_V^{T=1} \\
F^2\Delta^\pi_{(2)} &= -2g_A^e\xi_V^n \sum_l \Re \\
&\times \{v_T[l(l+1)^2(\frac{3}{\sqrt{2}}M^{0*}_{l+}M^{\frac{1}{2}}_{l+} - 3|M^0_{l+}|^2) + l^2(l+1)(\frac{3}{\sqrt{2}}M^{0*}_{l-}M^{\frac{1}{2}}_{l-} - 3|M^0_{l-}|^2)
\end{aligned}$$

$$
\begin{aligned}
&+ \quad (l+2)(l+1)^2(\frac{3}{\sqrt{2}}E^{0*}_{l+}E^{\frac{1}{2}}_{l+} - 3|E^0_{l+}|^2) + l^2(l-1)(\frac{3}{\sqrt{2}}E^{0*}_{l-}E^{\frac{1}{2}}_{l-} - 3|E^0_{l-}|^2)] \\
&+ \quad v_L[(l+1)^3\frac{3}{\sqrt{2}}S^{0*}_{l+}S^{\frac{1}{2}}_{l+} - 3|S^0_{l+}|^2) + l^3(\frac{3}{\sqrt{2}}S^{0*}_{l-}S^{\frac{1}{2}}_{l-} - 3|S^0_{l-}|^2)]\} \qquad (29) \\
F^2\Delta^{\pi}_{(3)} &= 2g^e_V v_{T'} \sum_l \Re\{l(l+1)^2\tilde{E}^{5*}_{l+}M_{l+} - (l+1)^2(l+2)\tilde{M}^{5*}_{l+}E_{l+} \\
&- \quad l^2(l+1)\tilde{E}^{5*}_{l-}M_{l-} + l^2(l-1)\tilde{M}^{5*}_{l-}E_{l-}\},
\end{aligned}
$$

where the E's, M's, and S's are transverse electric, transverse magnetic, and longitudinal multipoles, respectively [12, 38, 39], their subscripts denote the angular momentum and parity, their superscripts indicate the isospin decomposition,

$$
\begin{aligned}
v_T &= \frac{1}{2}|\frac{Q^2}{q^2}| + \tan^2\frac{\theta_e}{2} \\
v'_T &= \tan\frac{\theta_e}{2}\sqrt{|\frac{Q^2}{q^2}| + \tan^2\frac{\theta_e}{2}} \qquad (30) \\
v_L &= |\frac{Q^2}{q^2}|^2,
\end{aligned}
$$

and F^2 corresponds to the inclusive electromagnetic cross section, normalized to the Mott cross section (in the notation used here, F^2 corresponds to $2W_1^{EM}\sin^2\frac{\theta_e}{2} + W_2^{EM}\cos^2\frac{\theta_e}{2}$). The conversion of coupling constants has been given in Ref. [37], where they find

$$
\begin{aligned}
g^e_A\xi^{T=1}_V &= -2\tilde{\alpha}, \\
-2g^e_A\xi^n_V &= -2(\tilde{\alpha} - 3\tilde{\gamma}).
\end{aligned}
$$

Also, we note that the axial contribution, $F^2\Delta^{\pi}_{(3)}$, has no isospin decomposition given here. The contributions to this term, however, come from three sources [40]: the dominant isovector piece, which includes the axial transition form factor $G^A_{N\Delta}(Q^2)$; the primordial weak isoscalar axial current, which vanishes in the minimal $\mathrm{SU}(2)_L\times\mathrm{U}(1)$ standard model (and becomes nonvanishing only when weak radiative corrections are included); and the heavy quark isoscalar axial currents, which were originally neglected in writing down the phenomenological Lagrangian for electron nucleon scattering (denoted by dots in Eq. (5)), and are expected to be only a few percent of the isovector contribution [40]. Thus, for a first generation inelastic channel parity violation measurement, the axial term may be taken to have a contribution only from the isovector piece containing the axial transition form factor $G^A_{N\Delta}(Q^2)$ [40]. Thus, we may write

$$
A^{\pi}_{RL} = \frac{G_F}{\sqrt{2}}\frac{Q^2}{q\pi\alpha}[\tilde{\alpha} + (\tilde{\alpha} - 3\tilde{\gamma})\Delta^{\pi'}_{(2)} + \tilde{\beta}F(Q^2, E, E', \theta_e)], \qquad (31)
$$

where $F(Q^2, E, E', \theta_e)$ is given by Eq. (7) and in Appendix A, and

$$
\Delta^{\pi'}_{(2)} = \frac{\Delta^{\pi}_{(2)}}{-2(\tilde{\alpha} - 3\tilde{\gamma})}. \qquad (32)
$$

As can be seen from Eq. (29), there are an infinite number of multipoles which comprise the non-resonant background contribution to the 1 pion electroproduction asymmetry, with

both isovector and isoscalar pieces. Thus, even in keeping only the leading order multipoles implies that an isospin decomposition is necessary to describe the non-resonant contribution. As discussed earlier, an extensive data base for photoproduction from both the proton and neutron [41, 42, 43, 44, 45, 46] exist, and complete multipole and isospin decompositions have been done at the photon point [**?**, **?**]. Such a decomposition does not exist for finite Q^2, as electroproduction data on neutron targets is quite limited. Once the analysis on the data from Hall B [21] are analyzed, a more thorough description of the background will be possible.

References

[1] D.H. Beck, Phys. Rev. D **39**, 3248 (1989).

[2] L.M. Nath, K. Schilcher, and M. Kretzschmar, Phys. Rev. D **25**, 2300, 1982.

[3] W. Rarita and J. Schwinger, Phys. Rev. **60**, 61 (1941).

[4] C.H. Llewellyn Smith, Phys. Rep. **3**, 261 (1972).

[5] Nimai C. Mukhopadhyay *et al.,* Nucl. Phys. **A633**, 481 (1998).

[6] D. Leinweber, T. Draper, and R.M. Woloshyn, PHys. Rev. **D 46**, 3067 (1992).

[7] T.R. Hemmert, B.R. Holstein, and Nimai C. Mukhopadhyay, Phys. Rev. D **51**, 158 (1995).

[8] B. Golli, L. Amoreira, M. Fiolhais, and S. Sirca, hep-ph/0211293.

[9] P.Q. Hung and J.J. Sakurai, Ann. Rev. Nucl. Part. Sci. **31**, 375 (1981).

[10] D.R.T. Jones and S.T. Petcov, Phys. Lett. B **91**, 137 (1980).

[11] R.N. Cahn and F.J. Gilman, Phys. Rev. D **17**, 1313 (1978)

[12] S.L. Adler, Ann. Phys. **50**, 189 (1968).

[13] S.J. Barish *et al.,* Phys. Rev. D **19**, 2521 (1979).

[14] T. Kitagaki *et al.,* Phys. Rev. D **42**, 1331 (1990).

[15] L. Elouadrhiri, CEBAF Experiment E94-005.

[16] P. Joos *et al.,* Phys. Lett. B **62**, 230 (1976).

[17] S. Choi *et al.,* Phys. Rev. Lett. **71**, 3927 (1993).

[18] S.L. Adler and W.I. Weisberger, Phys. Rev. **169**, 1392 (1968).

[19] H. Schmieden, Eur. Phys. J. **A1:** 427 (1998).

[20] T. Sato and T.-S.H. Lee, nucl-th/0010025 (2000).

[21] V. Burkert in N^* *WORKSHOP* - "Partial Wave Analysis," CEBAF, Nov. 9-12, 1995.

[22] Shi-Lin Zhu, C.M. Mackawa, G. Sacco, B.R. Holstein, and M.J. Ramsey-Musolf, hep-ph/0107076.

[23] Y. Hara, Phys. Rev. Lett. **12**, 378 (1964).

[24] B. Borasoy and B.R. Holstein, Phys. Rev. **D 59**, 094025, and hep-ph/9902431.

[25] B. Desplanques, J.F. Donoghue, and B.R. Holstein, Ann. Phys. **124**, 449 (1980).

[26] Shi-lin Zhu, S.J. Publia, B.R. Holstein, and M.J. Ramsey-Musolf, hep-ph/0012253.

[27] H.-W. Hammer and D. Drechsel, Z. Phys. **A353**, 321 (1995).

[28] S.P. Wells, LATECH-CAPS-99-03b, G0-99-008, (1999).

[29] C. Murphy, S.P. Wells, and N. Simicevic, LATECH-CAPS-99-11a, G0-99-051, (1999).

[30] J. W. Lightbody and J. S. O'Connel, Computers in Physics **2**, 57 (1988).

[31] F. W. Brasse *et al.,* Nucl. Phys. B **110**, 413 (1976).

[32] F. W. Brasse *et al.,* NC **55A**, 679 (1967).

[33] F. James and M. Roos, CERN computer center program, (1977).

[34] G0 Technical Design Report, Nuclear Physics Laboratory,

[35] M. Pitt and J. Roche, private communication.

[36] S.M. Seltzer and M.J. Berger, Nucl. Instr. and Meth. B **12**, 95 (1985).

[37] M.J. Musolf, T.W. Donnelly, J. Dubach, S.J. Pollock, S. Kowalski, and E.J. Beise, Phys. Rep. **239**, 1 (1994).

[38] S.J. Pollock, Ph.D. Thesis, Stanford University (1987) unpublished.

[39] A.S. Raskin and T.W. Donnelly, Ann. Phys. **191**, 78 (1989).

[40] T.W. Donnelly, private communication.

[41] W. Pfeil and D. Schwela, Nucl. Phys. B **45**, 379 (1971).

[42] F.A. Berends and A. Donnachie, Nucl. Phys. B **84**, 342 (1975).

[43] S. Suzuki, S. Kurokawa, and K. Kondo, Nucl. Phys. B **68**, 413 (1974).

[44] I.I. Miroshnichenko *et al.,* Sov. J. Nucl. Phys. **32**, 339 (1980).

[45] V.A. Get'man *et al.,* Sov. J. Nucl. Phys. **38**, 230 (1983).

[46] V.F. Grushin *et al.,* Sov. J. Nucl. Phys. **38**, 881 (1983).